INTERNATIONAL JOURNAL FOR NUMERICAL METHODS IN BIOMEDICAL ENGINEERING
Int. J. Numer. Meth. Biomed. Engng. 2013; **29**:83–103
Published online 27 June 2012 in Wiley Online Library (wileyonlinelibrary.com). DOI: 10.1002/cnm.2497

Structure-based finite strain modelling of the human left ventricle in diastole

H. M. Wang [1], H. Gao [2], X. Y. Luo [2,*,†], C. Berry [3], B. E. Griffith [4], R. W. Ogden [2,5] and T. J. Wang [1]

[1] *SV Lab, School of Aerospace Engineering, Xi'an Jiaotong University, Xi'an 710049, People's Republic of China*
[2] *School of Mathematics and Statistics, University of Glasgow, Glasgow, UK*
[3] *Institute of Cardiovascular and Medical Sciences, University of Glasgow, Glasgow, UK*
[4] *Leon H. Charney Division of Cardiology, Department of Medicine, New York University School of Medicine, New York, NY, USA*
[5] *School of Engineering, University of Aberdeen, King's College, Aberdeen, UK*

SUMMARY

Finite strain analyses of the left ventricle provide important information on heart function and have the potential to provide insights into the biomechanics of myocardial contractility in health and disease. Systolic dysfunction is the most common cause of heart failure; however, abnormalities of diastolic function also contribute to heart failure, and are associated with conditions including left ventricular hypertrophy and diabetes. The clinical significance of diastolic abnormalities is less well understood than systolic dysfunction, and specific treatments are presently lacking. To obtain qualitative and quantitative information on heart function in diastole, we develop a three-dimensional computational model of the human left ventricle that is derived from noninvasive imaging data. This anatomically realistic model has a rule-based fibre structure and a structure-based constitutive model. We investigate the sensitivity of this comprehensive model to small changes in the constitutive parameters and to changes in the fibre distribution. We make extensive comparisons between this model and similar models that employ different constitutive models, and we demonstrate qualitative and quantitative differences in stress and strain distributions for the different constitutive models. We also provide an initial validation of our model through comparisons to experimental data on stress and strain distributions in the left ventricle. Copyright © 2012 John Wiley & Sons, Ltd.

Received 2 March 2012; Revised 8 May 2012; Accepted 10 May 2012

KEY WORDS: left ventricle in diastole; constitutive law; fibre structure; finite element methods; nonlinear finite strain; MRI

1. INTRODUCTION

Cardiac diseases remain a major public health burden. For instance, in 2009 and 2010 there were 98,506 hospitalisations for acute coronary syndrome in the United Kingdom, and these were associated with a £9.6 billion societal loss (2011). Paradoxically, because of improvements in early survival post-myocardial infarction, an increasing number of people are living with injured hearts, and these patients are subject to an increased risk of subsequent heart failure and premature death [1]. Improvements in risk assessment are urgently needed to identify high-risk patients and to stratify therapeutic approaches. Epidemiological studies have shown that at least 50% of heart failure patients have normal systolic pump function and left ventricular ejection fraction; these patients are said to suffer from left ventricular diastolic dysfunction [2–4]. Theoretical, computational, and experimental analyses of the diastolic mechanics of the left ventricle (LV) can be used to develop an

*Correspondence to: X. Y. Luo, School of Mathematics and Statistics, University of Glasgow, Glasgow, UK.
[†]E-mail: xiaoyu.luo@glasgow.ac.uk

improved understanding of the physiology and pathophysiology of such patients, and could be used to predict their responses to medical and surgical interventions. However, such analyses are complicated by large tissue deformations and by the anisotropy and inhomogeneity of the left ventricular myocardium. Moreover, performing such analyses using *in vivo* human anatomy, as required to maximize impact on patient care, requires high-quality noninvasive imaging data that can be difficult to obtain.

The heart wall consists of three distinct layers: thin inner and outer layers (the endocardium and epicardium, respectively), and a thick middle layer (the myocardium). The myocardium is primarily composed of cardiomyocytes that are arranged in bundles of muscle fibres. The fibre orientation changes with position within the wall. In the equatorial region of the LV, the predominant fibre direction (with respect to the circumferential direction along the left ventricular wall) rotates from approximately -50° to -70° in the subepicardium, to nearly 0° in the mid-wall, to approximately $+50^\circ$ to $+70^\circ$ in the subendocardium [5]. Extensive histological studies [6–8] have suggested that the fibres of the left ventricular myocardium are organized as laminar sheets that are tightly bound by endomysial collagen and loosely bound by perimysial collagen. Although it is possible to determine the actual fibre and sheet orientations in *ex vivo* hearts, obtaining such data *in situ* remains challenging. Previous works have developed models of a mean fibre distribution using rule-based reconstructions [9, 10]. Although rule-based reconstructions can yield fibre structures that are reasonably close to those derived from diffusion tensor magnetic resonance imaging (DTMRI) data, discrepancies exist between rule-based and DTMRI-based fibre structures [9]. An important issue that we consider herein is the sensitivity of the LV model predictions to the details of the prescribed fibre structure.

Most experimental data available for the material properties of the LV come from animal models. For instance, biaxial tests on the passive elasticity of canine and porcine myocardium have been performed [11–14]. Results from a complete set of simple shear tests for porcine myocardium have also been described [15], and these experiments clearly demonstrate the strong anisotropic behaviour of the myocardium. Although some aspects of the passive mechanical response of myocardial tissue are well characterized, a careful literature survey shows that there are insufficient experimental data available for detailed parameter estimation for many constitutive laws used to model the LV. This is especially true of human myocardium, for which experimental data are largely lacking.

Experiments by Vossoughi *et al.* [16] showed that myocardial tissues are incompressible and can be considered to be hyperelastic. Initial constitutive models of ventricular myocardium used isotropic material descriptions [17]. Subsequent work developed transversely isotropic models to account for the anisotropy of the myocardium [18–22]. These constitutive models describe some of the key mechanical properties of myocardial tissues, but they do not account for the orthotropic character of soft tissues. One of the first orthotropic constitutive models of ventricular myocardium was the 18-parameter 'pole-zero' model of Hunter *et al.* [6]. Other orthotropic models were developed by Costa *et al.* [23] and by Schmid *et al.* [24], in which Fung-type (exponential) strain-energy functionals were used. These models, which are based on earlier transversely isotropic models, are partly structure-based and partly phenomenological. For an in-depth discussion of constitutive models for the passive elasticity of myocardial tissues, see [24, 25], and [5].

Overall, although various constitutive laws for cardiac muscle have been developed, most of these models rely on phenomenological descriptions of the complex fibre structure of the myocardium. Additionally, the material parameters of many of these models lack a clear physical meaning, and some of these parameters are highly correlated. Constitutive models that are entirely structure-based have also been developed, such as the model of Horowitz *et al.* [26], which considers changes in the waviness of the fibres induced by the tissue strain. This model is not well-suited for numerical implementation, however, and it is also effectively transversely isotropic. Recently, Holzapfel and Ogden proposed a new structure-based constitutive model of the ventricular myocardium that accounts for the locally orthotropic tissue microstructure by expressing the strain energy functional using fibre-based material invariants [5]. In the incompressible case, their strain-energy functional has eight material parameters with relatively clear physical meanings. Moreover, this model satisfies convexity and strong ellipticity properties that are important both mathematically and physically.

DOI: 10.1002/cnm

Once the constitutive model is specified, the equilibrium equations are closed by choosing suitable boundary conditions, and these equations can be solved numerically to assess the strain and stress distributions in the left ventricular wall. Among the various numerical approaches currently used for such problems, the finite element (FE) method is arguably the most appropriate. There have been numerous earlier FE-based simulation studies of cardiac mechanics. Costa *et al.* [19] used prolate spheroidal coordinates and cubic Hermite elements to build a thick-walled ellipsoidal model of the passive mechanics of the LV. Vetter and McCulloch [27] studied the rabbit LV in diastole using a three-dimensional FE method. Nash and Hunter [28] developed an FE framework for large-deformation heart simulation using the pole-zero constitutive law. Stevens *et al.* [29] developed a three-dimensional heart model based on anatomic data from the porcine heart and performed numerical simulations using that model. They also evaluated the sensitivity of material parameters of the pole-zero constitutive law and found that the parameters of this model are coupled, primarily through the incompressibility constraint. These observations suggested that the pole-zero law might need to be reformulated to achieve a better separation of material parameters associated with deviatoric stresses.

In this work, we model left ventricular diastolic mechanics using a structure-based constitutive model of the LV in conjunction with human anatomical geometry obtained from noninvasive imaging studies. Following the framework of Holzapfel and Ogden [5], we treat the left ventricular myocardium as an inhomogeneous, thick-walled, nonlinearly elastic, incompressible material. We use cardiac magnetic resonance imaging (MRI) to determine the geometry of the LV, which can be reasonably reconstructed from routine clinical imaging studies. In principle, the cardiac fibre structure and other material parameters of the heart can be determined by advanced imaging methods; however, in the current model, we use a rule-based fibre structure along with material parameters derived from experimental data from the porcine heart. Discrete versions of the governing equations are solved using the nonlinear finite element software ABAQUS FEA (Simulia, Providence, RI, USA).

Using this computational model, we consider the sensitivity of the LV model to curve fitting errors that can occur when parameterizing the constitutive law using experimental data, and we find that the predictions of the LV model are relatively insensitive to such errors. We also identify the effects of changes in the underlying fibre structure on the stress or strain distributions within the LV wall. Our results show that the model results are sensitive to such changes, thereby suggesting that realistic patient-specific fibre structures should be used in future clinical applications of this or similar models. Model predictions obtained using the structure-based constitutive law are also compared with predictions obtained with Fung-type constitutive models, and large differences are observed between the two constitutive modelling approaches. Comparisons are also made between the model results and earlier experimental results. These experimental data are primarily for the canine heart, however, and only a general qualitative agreement is demonstrated.

2. CONSTITUTIVE LAW FOR THE PASSIVE MYOCARDIUM

Consider a continuum body with reference configuration $\mathcal{B}_0 \subset \mathbb{R}^3$ and current configuration $\mathcal{B}_t \subset \mathbb{R}^3$. These configurations are related by a time-dependent mapping $\boldsymbol{\chi} : \mathcal{B}_0 \times [0, T] \to \mathcal{B}_t$. Letting $\mathbf{X} \in \mathcal{B}_0$ denote coordinates in the reference configuration and $\mathbf{x} \in \mathcal{B}_t$ denote coordinates in the current configuration, the deformation gradient tensor associated with the motion $\mathbf{x} = \boldsymbol{\chi}(\mathbf{X}, t)$ is $\mathbf{F} = \partial \boldsymbol{\chi} / \partial \mathbf{X}$.

The constitutive model is described in terms of invariants of the right Cauchy–Green deformation tensor $\mathbf{C} = \mathbf{F}^{\boldsymbol{T}} \mathbf{F}$. The principal invariants of $\mathbf{C}$ are

$$I_1 = tr(\mathbf{C}), I_2 = \frac{1}{2}\left[I_1^2 - \mathrm{tr}\left(\mathbf{C}^2\right)\right], I_3 = \det(\mathbf{C}) \tag{1}$$

Because we model the ventricular myocardium as an incompressible material, we require that $J = \det(\mathbf{F}) = 1$; hence, $I_3 = 1$. The LV fibre structure is described by the fibre axis $\mathbf{f}_0$, the sheet (cross-fibre) axis $\mathbf{s}_0$, and the sheet-normal axis $\mathbf{n}_0 = \mathbf{f}_0 \times \mathbf{s}_0$; see Figure 1.

DOI: 10.1002/cnm

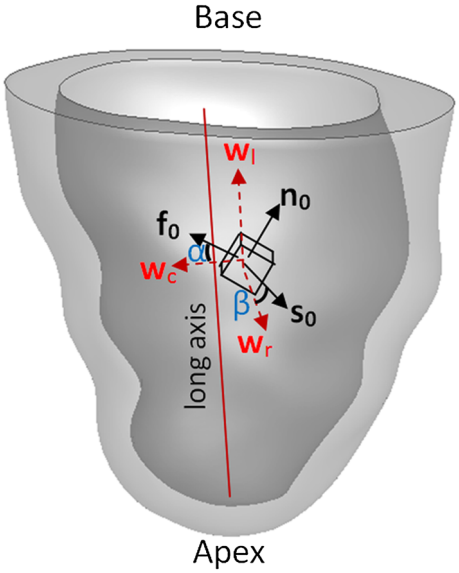

Figure 1. The fibre-aligned material axes and the local coordinate axes of the left ventricle, in which $(\mathbf{f_0}, \mathbf{s_0}, \mathbf{n_0})$ are the fibre, sheet, and sheet-normal axes, as described in the text, and in which $(\mathbf{w}_c, \mathbf{w}_l, \mathbf{w}_r)$ are coordinate axes that indicate the local circumferential, longitudinal and radial axes. The helix angle α is defined to be the angle between $\mathbf{f}_0$ and $\mathbf{w}_c$ in the plane spanned by $\mathbf{w}_c$ and $\mathbf{w}_l$, and the sheet angle β is defined to be the angle between $\mathbf{s}_0$ and $\mathbf{w}_r$ in the plane spanned by $\mathbf{w}_l$ and $\mathbf{w}_r$.

Using these material axes, additional quasi-invariants can be defined to characterize the material response in these preferred directions. In this work, we shall use the fibre, sheet, and fibre-sheet invariants

$$I_{4\mathrm{f}} = \mathbf{f}_0 \cdot (\mathbf{C}\mathbf{f}_0)\,, I_{4\mathrm{s}} = \mathbf{s}_0 \cdot (\mathbf{C}\mathbf{s}_0)\,, I_{8\mathrm{fs}} = \mathbf{f}_0 \cdot (\mathbf{C}\mathbf{s}_0)\,. \tag{2}$$

Following Holzapfel and Ogden [5], the structure-based strain energy function is

$$\begin{aligned} W\left(I_1, I_{4\mathrm{f}}, I_{4\mathrm{s}}, I_{8\mathrm{fs}}\right) = &\frac{a}{2b}\exp\left[b\left(I_1-3\right)\right] \\ &+ \sum_{i=\mathrm{f,s}} \frac{a_i}{2b_i}\left\{\exp\left[b_i\left(I_{4i}-1\right)^2\right]-1\right\} \\ &+ \frac{a_{\mathrm{fs}}}{2b_{\mathrm{fs}}}\left\{\exp\left[b_{\mathrm{fs}}\left(I_{8\mathrm{fs}}\right)^2\right]-1\right\} \end{aligned} \tag{3}$$

in which a, b, a_i, b_i $(i = \mathrm{f}, \mathrm{s}, \mathrm{fs})$ are eight non-negative material parameters. The first term is a Fung-type expression that corresponds to the contributions to the strain energy of an isotropic ground matrix material. The remaining terms correspond to the contributions from the myocytes and from of families of collagen fibres embedded within the tissue. Because we assume that the collagen fibres support only extension and not compression, the terms involving I_{4i} for $i = \mathrm{f}, \mathrm{s}$ are included in the total energy only if $I_{4i} > 1$.

From Equation (3), the Cauchy stress tensor is determined by

$$\begin{aligned} \boldsymbol{\sigma} = &\mathbf{F}\sum_{i=1,4\mathrm{f},4\mathrm{s},8\mathrm{fs}} \frac{\partial W}{\partial I_i}\frac{\partial I_i}{\partial \mathbf{F}} - p\mathbf{I} = -p\mathbf{I} + a\exp\left[b\left(I_1-3\right)\right]\mathbf{B} \\ &+ 2a_{\mathrm{f}}\left(I_{4\mathrm{f}}-1\right)\exp\left[b_{\mathrm{f}}\left(I_{4\mathrm{f}}-1\right)^2\right]\mathbf{f}\otimes\mathbf{f} \\ &+ 2a_{\mathrm{s}}\left(I_{4\mathrm{s}}-1\right)\exp\left[b_{\mathrm{s}}\left(I_{4\mathrm{s}}-1\right)^2\right]\mathbf{s}\otimes\mathbf{s} \\ &+ a_{\mathrm{fs}}I_{8\mathrm{fs}}\exp\left[b_{\mathrm{fs}}\left(I_{8\mathrm{fs}}\right)^2\right](\mathbf{f}\otimes\mathbf{s}+\mathbf{s}\otimes\mathbf{f})\,, \end{aligned} \tag{4}$$

DOI: 10.1002/cnm

in which p is a Lagrange multiplier introduced to enforce the incompressibility constraint, $\mathbf{I}$ is the identity tensor, $\mathbf{B} = \mathbf{F}\mathbf{F}^{\boldsymbol{T}}$ is the left Cauchy–Green deformation tensor, and $\mathbf{f} = \mathbf{F}\mathbf{f}_0$ and $\mathbf{s} = \mathbf{F}\mathbf{s}_0$ are respectively the fibre and sheet axes in the current (i.e., deformed) configuration.

3. LEFT VENTRICULAR ANATOMICAL GEOMETRY

A cardiac magnetic resonance imaging study was performed on a healthy volunteer (male, age: 28) at the British Heart Foundation Glasgow Cardiovascular Research Centre using a Siemens Magnetom Avanto (Erlangen, Germany) 3.0 Tesla scanner with an eight-element phased array cardiac surface coil. The study protocol was approved by the local ethics committee, and written informed consent was obtained prior to the scan. A conventional cine MRI sequence was used. Study parameters for the short axis left ventricular slices were: flip angle=50°; echo time=1.51 ms; bandwidth=977 Hz/pixel; field of view=216 mm × 340 mm with matrix size of 216 × 256; and slice thickness = 10 mm. A four-chamber view long axis slice was also acquired to provide the structure of the apex.

Endocardial and epicardial boundaries were determined for seven short-axis slices at the end of diastole, which was identified by the peak of the R-wave in the subject's ECG (electrocardiogram). The resulting surfaces, which extend from the base of the LV to the apex, were manually delineated by a custom MATLAB (The MathWorks, Inc., Natick, MA, USA) script. Results from the segmentation are shown in Figure 2(a), and are superimposed on the long axis slice. The location of the apex was identified from the four-chamber view long axis slice. Following manual segmentation, the LV boundary points were imported into the SOLIDWORKS (SolidWorks Corp., Waltham, MA,

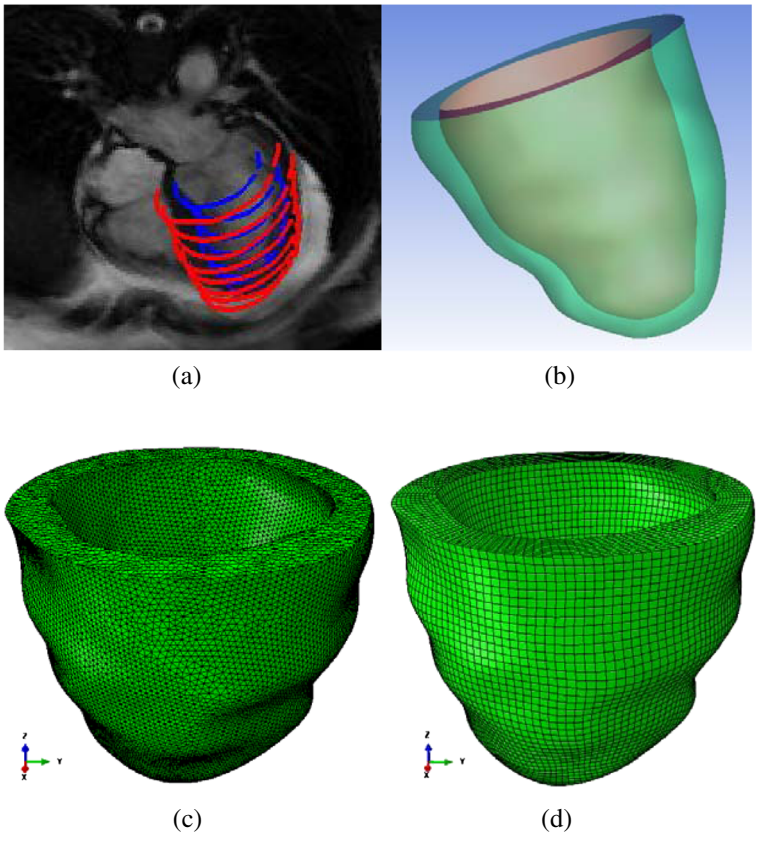

Figure 2. (a) LV boundary segmentation superimposed on a four-chamber view of the heart obtained from MRI imaging data; (b) the reconstructed LV geometry; (c) the tetrahedral mesh; and (d) the hexahedral mesh.

DOI: 10.1002/cnm

USA) software, which was used to reconstruct the LV geometry via B-spline surface fitting. The endocardial and epicardial boundaries are shown in Figure 2(b).

Data at the beginning of diastole were not available because the standard clinical MRI study does not cover the entire diastolic phase of the cardiac cycle. Because data were not available at the beginning of diastole, when myocardial stresses are presumably minimized, we use this end-diastolic configuration as our initial configuration to model the passive response of the LV to diastolic pressure loads.

4. RULE-BASED MYOCARDIAL FIBRE GENERATION

The anisotropic properties of myocardium play an important role in cardiac mechanics, and a physiologically accurate reconstruction of the myocardial fibre structure is an essential component of a realistic model of the heart. In the present study, *in vivo* data to determine the myocardial fibre orientation were not available. Hence, a rule-based myocardial fibre generation algorithm, based on the work of Potse *et al.* [10], was adopted. At each node of the FE LV mesh, two intramural distances are determined: d_{endo} and d_{epi}, the distances from the node to the endocardial and epicardial surfaces, respectively, along straight lines passing through the node that are normal to those surfaces. A normalized thickness parameter e is then defined for each node of the FE mesh by

$$e = \frac{d_{\text{endo}}}{d_{\text{endo}} + d_{\text{epi}}}. \tag{5}$$

Notice that by construction, $e = 0$ along the endocardial surface, and $e = 1$ along the epicardial surface.

The local cardiac coordinate system $(\mathbf{w}_{\text{c}}, \mathbf{w}_{\text{l}}, \mathbf{w}_{\text{r}})$ is defined so that $\mathbf{w}_{\text{c}}$ is the circumferential direction (circumferential with respect to the global apex-to-base axis of the chamber); $\mathbf{w}_{\text{r}}$ is the radial direction, which is oriented to point transmurally from the endocardial surface towards the epicardial surface; and $\mathbf{w}_{\text{l}} = \mathbf{w}_{\text{r}} \times \mathbf{w}_{\text{c}}$; see Figure 1. To account for transmural rotation in the fibre direction, a spatially varying helix angle α, which is the angle between the fibre axis $\mathbf{f_0}$ and the circumferential axis $\mathbf{w}_{\text{c}}$ in the plane spanned by $\mathbf{w}_{\text{c}}$ and $\mathbf{w}_{\text{l}}$ (see Figure 1), is defined for each element in the mesh via

$$\alpha = R(1 - 2\bar{e}_{\text{av}})^n,$$

in which R is the maximum fibre angle on the endocardial surface, $\bar{e}_{\text{av}}$ is the average value of e at the nodes of the element in question, and n is an empirically determined constant. Notice that so long as n is an odd integer, α takes the value $-R$ on the epicardial surface. Unless specified otherwise, R is set to be 60°, which we take to correspond to a normal fibre structure. The study of Bishop *et al.* [9] demonstrated that a rule-based linear method with $n = 1$ provides a closer match to DTMRI data than the value $n = 3$ used by Potse *et al.* [10]. Hence, in our study, n is set to equal 1.

The sheet angle β, which is the angle between the sheet axis $\mathbf{s_0}$ and the radial axis $\mathbf{w}_{\text{r}}$ in the plane spanned by $\mathbf{w}_{\text{r}}$ and $\mathbf{w}_{\text{l}}$ (see Figure 1), is determined similarly via

$$\beta = T(1 - 2\bar{e}_{\text{av}}),$$

in which T is the maximum sheet angle on the endocardial surface. Following LeGrice *et al.* [6], T is set so that the sheet angle varies from 45° on the endocardial surface to −45° on the epicardial surface.

Figure 3(a) shows myocardial fibres for each element at the endocardial and epicardial surfaces. Fibre paths shown in Figure 3(b) clearly illustrate the transmural change in fibre orientation.

5. FINITE ELEMENT MODEL OF PASSIVE LEFT VENTRICULAR MECHANICS

The computational approach that we adopt to model the passive mechanics of the LV is based on the classical pressure-dilatation-displacement three-field formulation commonly used to overcome

DOI: 10.1002/cnm

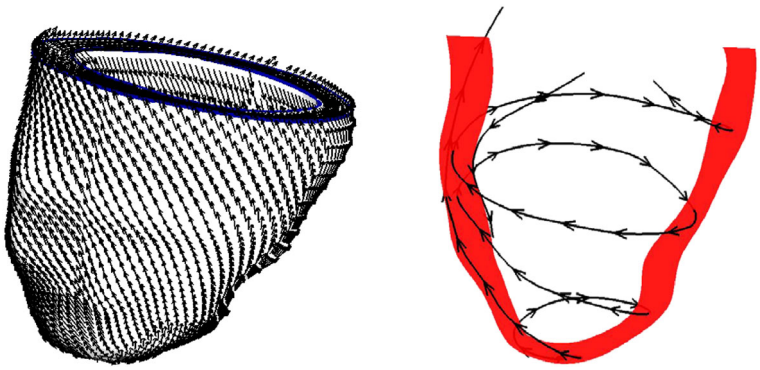

(a) (b)

Figure 3. (a) Myocardial fibre axis vectors and (b) examples of fibre traces.

locking problems exhibited by purely displacement-based finite element formulations of incompressible elasticity. Here we briefly introduce the decoupled volumetric-isochoric formulation of finite elasticity.

Following Miehe [30] and Göktepe *et al.* [31], among many others, we decompose the deformation gradient $\mathbf{F}$ into volumetric ($\mathbf{F}_{\mathbf{vol}}$) and isochoric ($\bar{\mathbf{F}}$) parts, that is,

$$\mathbf{F} = \bar{\mathbf{F}}\mathbf{F}_{\text{vol}},\ \mathbf{F}_{\text{vol}} = J^{1/3}\mathbf{I},\ \bar{\mathbf{F}} = J^{-1/3}\mathbf{F}\,, \tag{6}$$

in which $J = \det(\mathbf{F})$ and $\det(\bar{\mathbf{F}}) = 1$. The principle of virtual work is stated in the classical form as

$$\delta W_I = \int_V \boldsymbol{\sigma} : \delta\mathbf{D}\,\mathrm{d}V = \int_{V_0} \mathrm{J}\boldsymbol{\sigma} : \delta\mathbf{D}\,\mathrm{d}V_0 = \int_S \delta\mathbf{v}\cdot\mathbf{t}\,\mathrm{dS} + \int_V \delta\mathbf{v}\cdot\mathbf{f}\,\mathrm{d}V, \tag{7}$$

in which V and V_0 indicate volumes in the current and reference configurations, respectively, S is the surface of V, $\delta\mathbf{D}$ is the virtual rate of deformation, $\mathbf{t}$ is the stress vector, $\mathbf{f}$ is the body force, and $\delta\mathbf{v}$ is the virtual displacement. The internal virtual work per unit volume in the reference configuration, δW_I, can be written as

$$\delta W_I = \int_{V_0} \delta W\,\mathrm{d}V_0 = \int_{V_0} \left[\mathrm{J}\left((\boldsymbol{\sigma} + p\mathbf{I}) : \delta\mathbf{e} - p\delta\boldsymbol{\epsilon}^{\mathrm{vol}}\right) - (J-1)\delta p\right]\,\mathrm{dV}_0, \tag{8}$$

in which $\delta\boldsymbol{\epsilon}^{\mathbf{vol}} = \mathbf{I} : \delta\mathbf{D}$ is the virtual volumetric strain rate, $\delta\mathbf{e} = \delta\mathbf{D} - \frac{1}{3}\delta\boldsymbol{\epsilon}^{\mathrm{vol}}\mathbf{I}$ is the virtual deviatoric strain rate, and δW and δp are variations of W and p, which are defined in Equations (3) and (4), respectively. This formulation is implemented in the general-purpose finite element program ABAQUS via a user-defined UANISOHYPER_INV subroutine.

To constrain the motion of the model, the longitudinal displacement of the base and the circumferential displacement of the epicardial wall at the base are set to zero. The remainder of the left ventricular wall, including the apex, is left free. A pressure load, generally varying from 0 to 8 mmHg, is applied on the endocardial surface. Such loads are typical physiological end-diastolic pressures. We assume the reference configuration, which is derived from imaging data obtained at end-diastole, to be a stress-free configuration. Because of the presence of *in vivo* pressure loads and residual stresses, however, this configuration would not actually be stress-free in a real heart. The impact of initial strains and residual stresses on the mechanical behaviour of the LV in diastole will be addressed in future work.

We compare results produced by the model when using a tetrahedral mesh composed of 322,827 elements and 62,559 nodes to results obtained on a hexahedral mesh composed of 48,050 elements and 53,548 nodes. These meshes are shown in Figure 2 panels (c) and (d), respectively. Differences in the results are small; the maximum displacements are almost identical, and the maximum stresses

DOI: 10.1002/cnm

in the fibre direction have a relative difference of less than 3%. Because hexahedral elements generally offer superior stability and accuracy for problems of incompressible elasticity, we employ the hexahedral mesh in all subsequent computations.

We use the three-dimensional hybrid C3D8H isoparametric element implemented in ABAQUS, which yields trilinear displacements and piecewise-constant pressures (Q1P0). Numerical quadrature is performed using a 2×2×2 Gauss rule. The discretised form of Equation (8) is solved iteratively using Newton's method.

6. SIMULATION RESULTS

6.1. Sensitivity to the material parameters in the constitutive law

Following Holzapfel and Ogden [5] and Göktepe *et al.* [31], we estimate the eight material parameters $a, b, a_i, b_i (i = \text{f, s, fs})$ in the constitutive model stated in Equation (3) using data from simple shear tests on porcine ventricular myocardium reported by Dokos *et al.* [15]. Because Holzapfel and Ogden [5] and Göktepe *et al.* [31] obtained somewhat different constitutive parameters using the same experimental data, we decided to construct our own parameter fit, which yields yet another set of model parameters from this same dataset.

Table I. Different fits of material parameters to data of Dokos *et al.* [15].

a (kPa)	b	a_f (kPa)	b_f	a_s (kPa)	b_s	a_fs (kPa)	b_fs	Source
0.059	8.023	18.472	16.026	2.481	11.120	0.216	11.436	[5]
0.496	7.209	15.193	20.417	3.283	11.176	0.662	9.466	[31]
0.2362	10.810	20.037	14.154	3.7245	5.1645	0.4108	11.300	Present

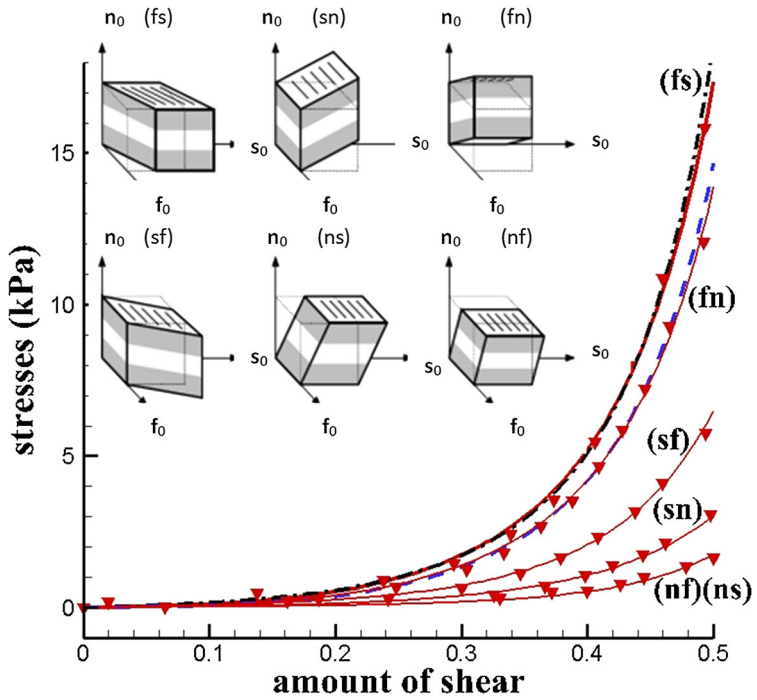

Figure 4. Experimental data of Dokos *et al.* [15] in the six simple shear directions (as indicated by the insert) and results from the parameterized structure-based constitutive law. The symbols are from the experimental data, and the red solid curves correspond to results obtained using the parameterization determined herein. The thicker solid line (red) is the present fitting for the (fs) curve, and the blue (dashed) and black (dashdot) curves are the (fs) curves by Holzapfel and Ogden [5] (H-O) and by Göktepe *et al.* [31] (G-K), respectively.

For clarity, comparisons of other curves from the H-O and G-K parameterizations are not shown.

DOI: 10.1002/cnm

To estimate the material parameters of the model, we minimize the objective function

$$\varphi(\kappa) = \sum_{ij} \sum_{k=1}^{N_{ij}^{(\exp)}} \left(\sigma_{ij} - \bar{\sigma}_{ij}^{(k)}\right)^2, \tag{9}$$

with respect to the material parameters, in which $\kappa = \{a, b, a_f, b_f, a_s, b_s, a_{fs}, b_{fs}\}$, σ_{ij} and $\bar{\sigma}_{ij}^{(k)}$ are the computed and measured stress components, respectively, and $N_{ij}^{(\exp)}$ is the total number of data points extracted from the shear test data. Here, (ij) refers to shear in the jth direction in the i-j plane, with $i, j \in \{f = 1, s = 2, n = 3\}$. With this notation, we subsequently shall identify σ_{11} as the stress in the fibre direction. For the planes containing the fibre axis, the shear responses in the sheet (fs) and sheet normal (fn) directions are different, and for the planes containing the sheet axis,

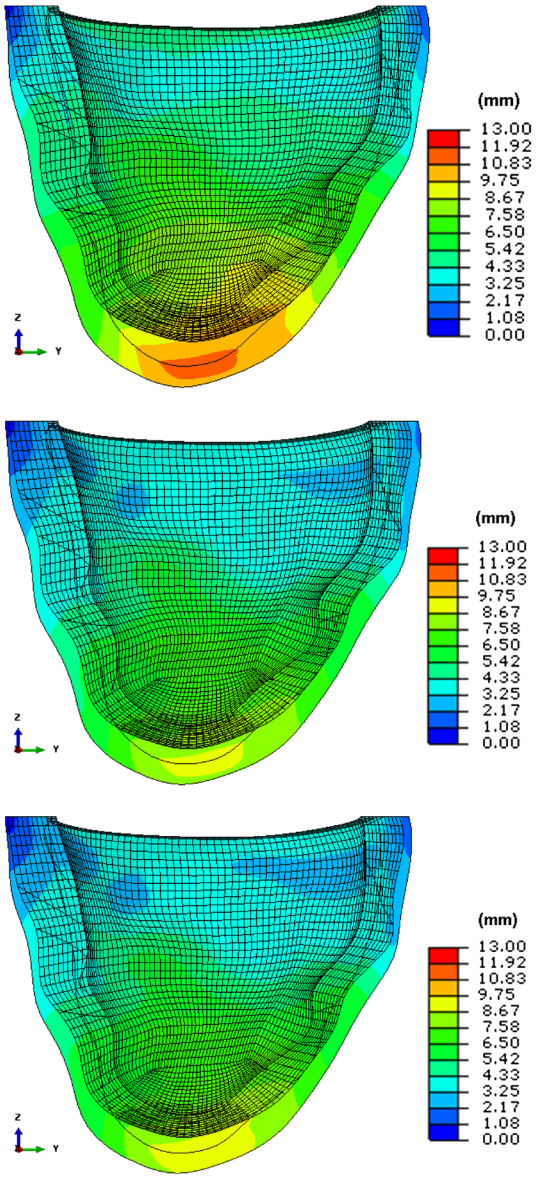

Figure 5. Distributions of displacement at a pressure load of 8 mmHg determined using parameters obtained by Holzapfel and Ogden [5] (top), for which $U^{\max} = 12.58$ mm; by Göktepe *et al.* [31] (middle), for which $U^{\max} = 9.87$ mm; and in the present work (bottom), for which $U^{\max} = 10.17$ mm.

DOI: 10.1002/cnm

the responses in the fibre (sf) and sheet normal (sn) directions are also different. The shear responses in the planes containing the sheet normal axis are the same for the specimen considered [5].

We solve the optimization problem via the Levenberg–Marquardt method. The material parameters identified from the experimental data are compared with those of previous studies in Table I.

Notice that, apart from the value of the parameter a, the three parameter sets are generally fairly similar. Because the constitutive law is defined so that the $I_{4\mathrm{f}}$ and $I_{4\mathrm{s}}$ terms have the major contributions to the stress, and because the parameters that influence these terms in the constitutive law are relatively close in all cases, we expect that the three parameter sets will yield similar results, as we

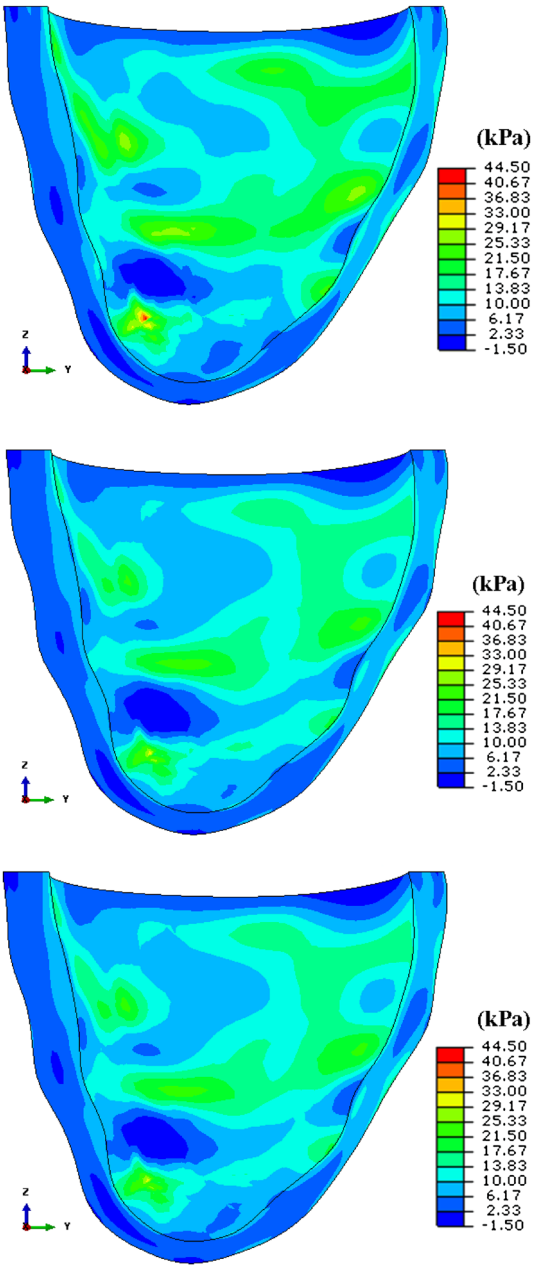

Figure 6. Distributions of stress in fibre direction σ_{11} at a pressure load of 8 mmHg determined using the parameters obtained by Holzapfel and Ogden [5] (top), for which $\sigma_{11}^{\max} = 44.07$ kPa; by Göktepe *et al.* [31] (middle), for which $\sigma_{11}^{\max} = 32.57$ kPa; and in the present work (bottom), for which $\sigma_{11}^{\max} = 31.68$ kPa.

DOI: 10.1002/cnm

indeed demonstrate below. The experimentally measured stress–strain curves of the six shear tests, along with the comparable stresses produced by the constitutive model, are shown in Figure 4.

The LV stress distributions and deformations using these three parameter sets are shown in Figures 5 and 6, respectively, for a loading pressure of 8 mmHg.

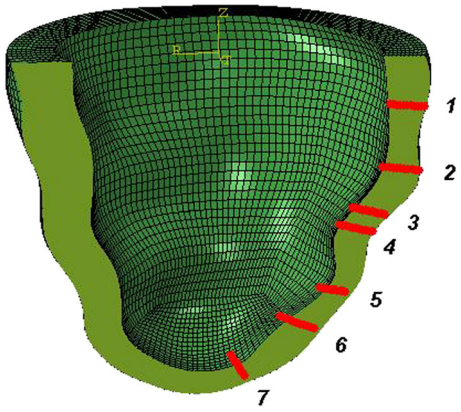

Figure 7. Locations of the seven paths across the LV free wall considered herein.

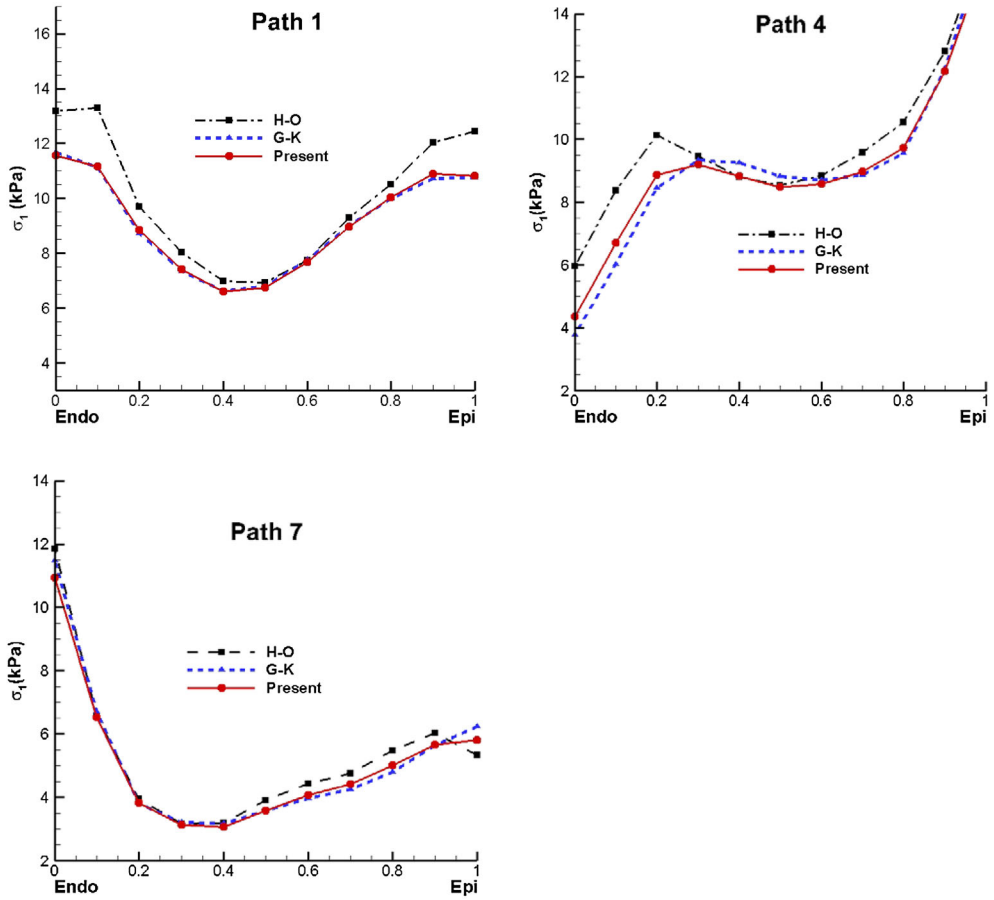

Figure 8. Transmural distribution of the first principal stress σ_1 along paths 1, 4 and 7, computed using the three parameter sets. Similar trends are predicted by all three sets of parameters. Agreement is especially close between results obtained using the parameterization determined herein and results obtained with the G-K parameter set.

DOI: 10.1002/cnm

These results indicate that the general stress distributions and displacements obtained when using the three sets of parameters are similar. The agreement is especially close between results obtained with the parameters of Göktepe *et al.* [31] (hereafter, G-K) and the results obtained using the parameters determined herein.

To facilitate a closer inspection of the results, we construct transmural paths across the LV free wall, as shown in Figure 7.

In Figure 8, we compare the distributions of the first principal stress σ_1 across the LV wall along paths 1, 4 and 7 for the three different parameter fittings at a loading pressure of 8 mmHg.

Again, all three parameter sets yield similar trends, with the closest agreement between results obtained using the G-K parameters and the parameter values determined herein. Hence, the differences between the parameter sets do not appear to have a major impact on the results of the three-dimensional model.

6.2. Transmural stress and strain distributions

Using the constitutive parameters determined in the present work, we investigate the mechanical behaviour of the LV in diastole. The transmural distributions of the stress in fibre direction σ_{11} and the logarithmic strain $\ln(\lambda_1)$, in which λ_1 is the stretch ratio in the fibre direction, along all eight paths (1–7) are shown in Figure 9. Notice that the stress and strain distributions are essentially uniform throughout most of the interior of the LV wall, and that the details of the stress and strain

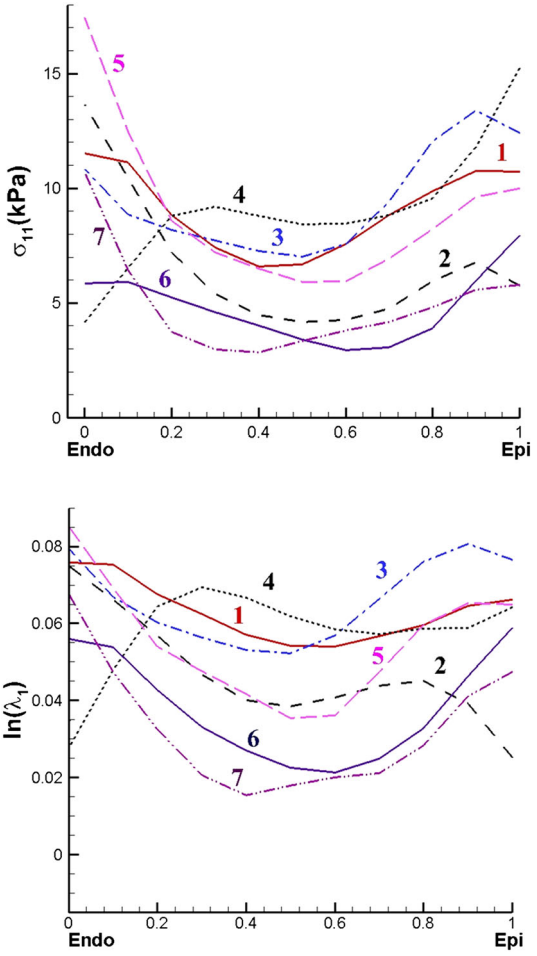

Figure 9. Transmural distributions of (a) stress in fibre direction σ_{11} and (b) logarithmic strain $\ln(\lambda_1)$ along paths 1–7, for the normal fibre structure.

DOI: 10.1002/cnm

levels and distribution trends are strongly path dependent. We remark that the distribution of the first principal stress σ_1 is very similar to that of the stress in the fibre direction (data not shown). This indicates that the principal stress is dominated by the fibre stress and is largely determined by the fibre orientation.

6.3. *Effect of variations in fibre distribution*

The structure of ventricular myocardium is highly inhomogeneous as a consequence of transmural fibre rotation and other regional differences. Although fibre angle distributions are qualitatively similar between healthy individuals, there are differences in fibre distributions between subjects. Fibre orientation may change in disease, including heart failure and myocardial infarction, as a consequence of pathological tissue remodelling [32]. Accurately determining the *in vivo* fibre orientation is difficult, however. Hence, it is important to quantify the sensitivity of left ventricular stress and strain distributions to changes in the fibre orientations. To this end, we consider eight different fibre structures:

(a) $R = 60°$, $T = 45°$ (normal fibre structure)
(b) $R = 60°$, $T = 30°$
(c) $R = 60°$, $T = 60°$
(d) $R = 30°$, $T = 45°$
(e) $R = 40°$, $T = 45°$
(f) $R = 50°$, $T = 45°$

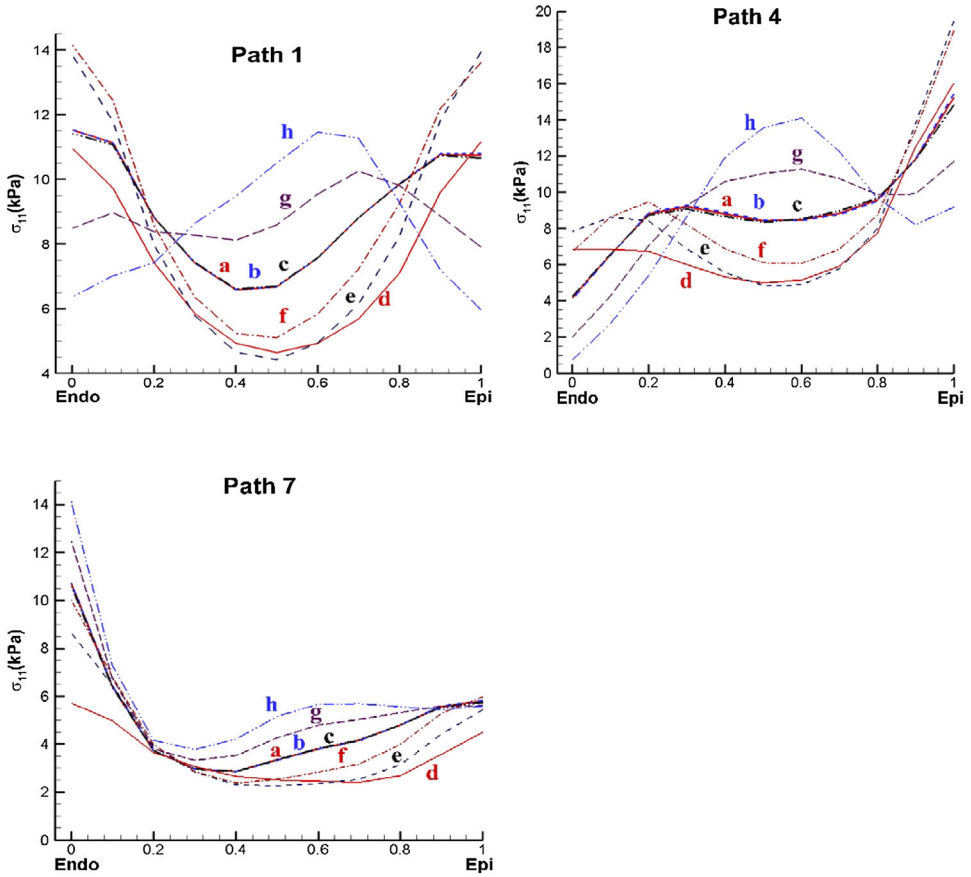

Figure 10. Transmural distributions of σ_{11}, the stress in fibre direction, along paths 1, 4 and 7 for different fibre and sheet angle combinations (a)–(h). Notice that the three curves corresponding to cases (a)–(c) nearly overlap.

DOI: 10.1002/cnm

(g) $R = 70°, T = 45°$
(h) $R = 80°, T = 45°$

The transmural distributions of σ_{11}, the stress in the fibre direction, along paths 1, 4 and 7 are shown in Figure 10 for these different fibre structures at a pressure load of 8 mmHg.

These results show that the transmural stress distribution is most sensitive to changes in maximal fibre angle near the base and equator (path 1), and least sensitive to such changes near the apex (path 7). Interestingly, changes in the maximal sheet orientation have virtually no impact on the transmural stress distributions, nor on the strain distributions (data not shown). This is in contrast to variations of the maximal fibre angle, which have large effects on the stress and strain distributions. This is because in diastole, the LV is expanding and the wall is thinning. Because the sheet axis is mostly aligned with the transmural direction, expansion reduces the effects of the invariant I_{4s} in the constitutive law, thereby minimizing contributions from coupling in the sheet direction on the overall stress state. As a result, the transmural distributions of stress and strain are essentially unchanged in cases (a)–(c).

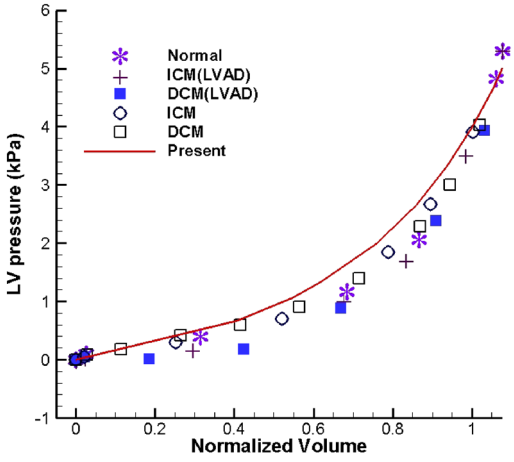

Figure 11. Comparisons of EDPVRs computed by our model and other experimental or computational models. (a) Comparisons to measurements from *ex vivo* human hearts [33]. Normal, healthy heart; ICM, ischemic cardiomyopathy; DCM, diopathic dilated cardiomyopathy; and LVAD, hearts supported by a left ventricular assist device. (b) Comparison to measurements for dog hearts from three experimental studies and one computational study.

DOI: 10.1002/cnm

6.4. *End-diastolic pressure–volume relationship*

As an initial validation of our model, we compare the end-diastolic pressure–volume relationship (EDPVR) generated by our model to experimental measurements from both human and canine hearts. Figure 11(a) compares the EDPVR of our model to EDPVR measurements from *ex vivo* human hearts [33] for both healthy tissue and for cases of ischemic cardiomyopathy. These curves are normalized as in [33] as $EDV_n = (EDV - V_0)/(V_{30} - V_0)$, in which V_0 is the volume when EDP is approximately 0 mmHg, which is 121 mL in the model, and V_{30} is the volume when EDP is approximately 30 mmHg, which is 194 mL in the model. As shown in Figure 11(a), there is good agreement between the model predictions and the human experimental data.

By contrast, comparisons to canine experimental data are less favourable. Figure 11b) compares our results to the EDPVR experimentally measured in canine hearts [34–36], but here scaling the relationship to indicate percentage increase in volume. The EDPVR generated by our model has a similar trend to these experimental measurements, but our model yields a somewhat stiffer pressure–volume response.

Given the good agreement in Figure 11(a), the differences between the model prediction and the experimental data in Figure 11(b) are likely a consequence of differences between the human and canine cardiac geometries. In fact, significant differences in the transmural stresses between human and canine hearts have been observed in experimental and simulation studies of Guccione and colleagues (private communication).

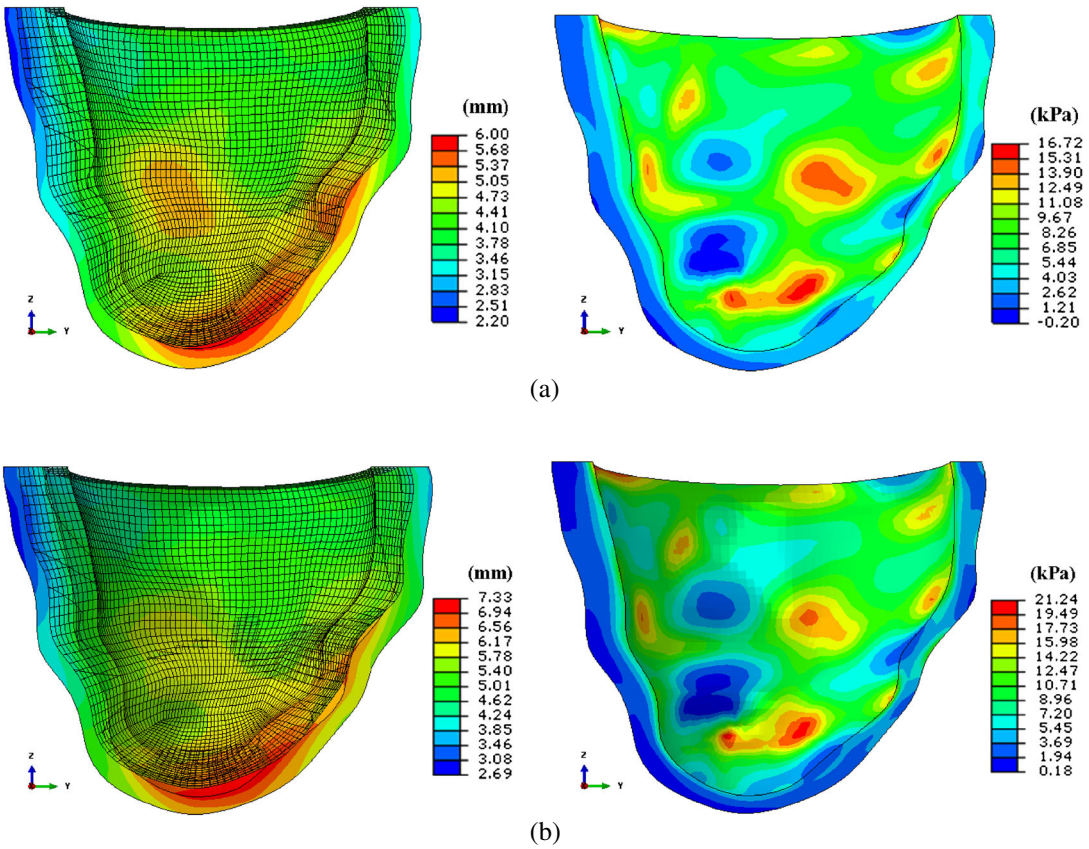

Figure 12. (a) Distributions of deformations (left panel) and fibre stresses (right panel) generated by the model for a pressure load of 8 mmHg when using the Costa constitutive model with parameters determined by Schmidt *et al.* [2008] from the experimental data of Dokos *et al.* [15]; and (b) similar to (a), but here using the Guccione constitutive model with parameters determined by Xi *et al.* [37] from the reparametrization of the Costa model by Schmidt *et al.* [2008].

DOI: 10.1002/cnm

6.5. Comparison to Fung-type models

Several commonly used Fung-type models treat the fibrous structure of the myocardium using an exponential strain energy functional of the form

$$W = \frac{1}{2}C(\exp(Q) - 1), \tag{10}$$

in which C is a constant and $Q = Q(\mathbf{F})$ is a function of various strain measures. For the canine LV, Guccione *et al.* [20] used a transversely isotropic model with

$$Q = b_1 E_{\mathrm{ff}}^2 + b_2\left(E_{\mathrm{cc}}^2 + E_{\mathrm{rr}}^2 + 2E_{\mathrm{cr}}E_{\mathrm{rc}}\right) + 2b_3(E_{\mathrm{fc}}E_{\mathrm{cf}} + E_{\mathrm{fr}}E_{\mathrm{rf}}), \tag{11}$$

in which $b_i\,(i = 1, 2, 3)$ are material parameters fit to experimental data, and E_{ij} are strain components referred to a system of local fibre, cross-fibre, and radial coordinates (f,c,r). Equations (10) and (11) specify a four-parameter Fung model referred to as the Guccione model. The popularity of this model is a consequence of its simplicity. Moreover, its four parameters may be uniquely determined and are relatively insensitive to experimental noise [37].

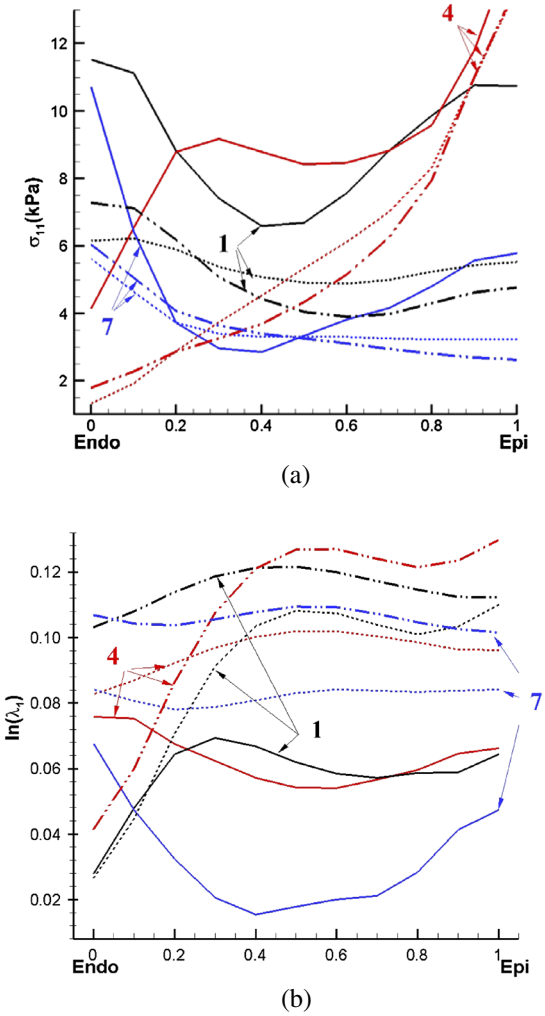

Figure 13. Comparison of transmural (a) stress and (b) logarithmic strain distributions obtained with the present LV geometry and fibre structure using the structure-based constitutive model (solid), the Guccione model (dash-dot-dot), and the Costa model (dotted) along paths 1, 4 and 7.

DOI: 10.1002/cnm

This constitutive law was extended to account for the orthotropic behaviour of ventricular myocardium by Costa *et al.* [23], who determine Q via

$$Q = b_{\mathrm{ff}}E_{\mathrm{ff}}^2 + b_{\mathrm{ss}}E_{\mathrm{ss}}^2 + b_{\mathrm{nn}}E_{\mathrm{nn}}^2 + 2b_{\mathrm{fs}}E_{\mathrm{fs}}^2 + 2b_{\mathrm{fn}}E_{\mathrm{fn}}^2 + 2b_{\mathrm{sn}}E_{\mathrm{sn}}^2, \tag{12}$$

in which the strain components E_{ij} are defined in a local Cartesian system with fibre-sheet-normal coordinates.

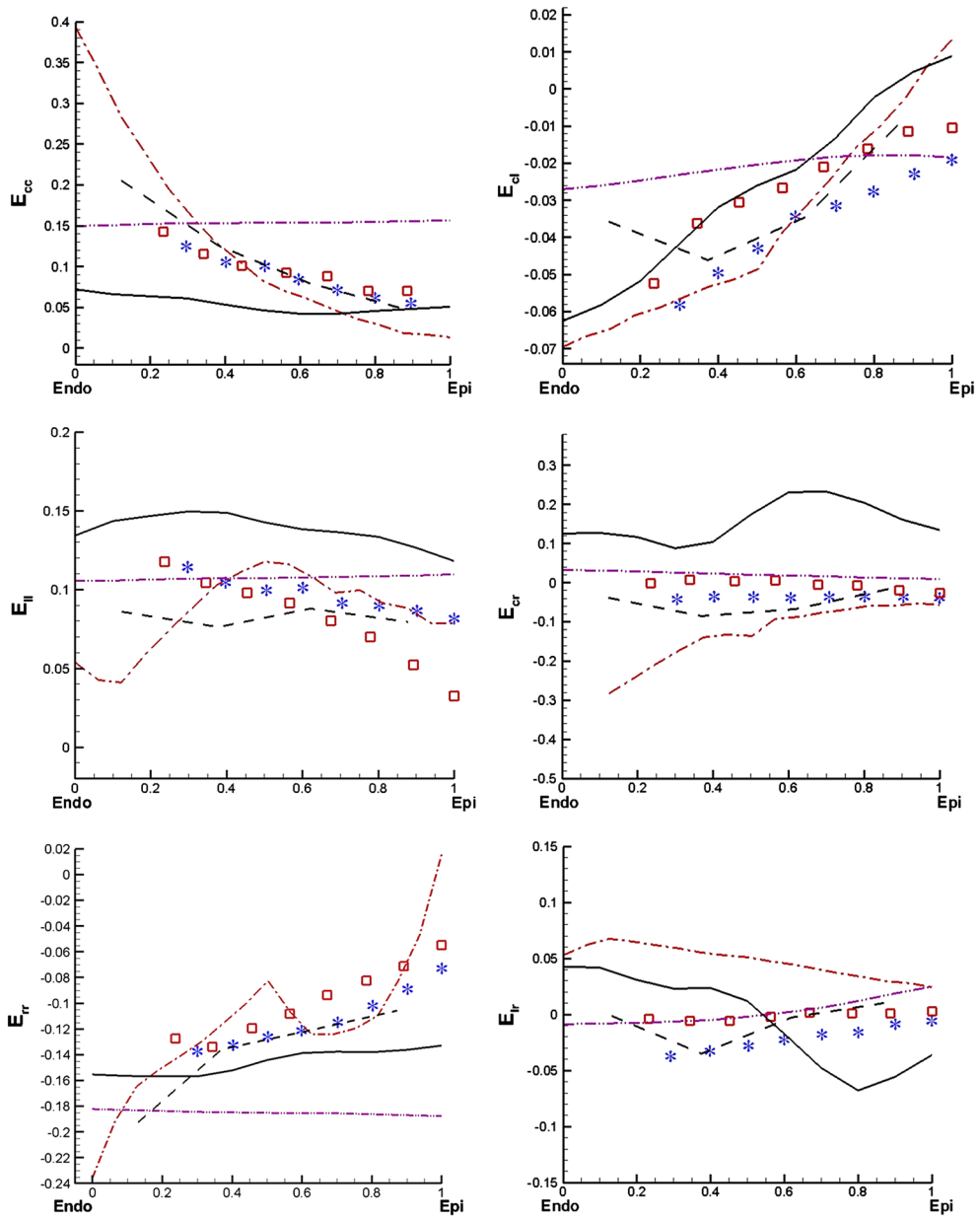

Figure 14. Transmural distributions of strain at a pressure load of 7.5 mmHg for the equatorial region of the anterior wall. Normal strain components are shown in the left column; shear strains are shown in the right column. The predictions of the present model along path 1 (solid) are compared with experimental observations of Omens *et al.* [36] (star; $n = 7$) and May-Newman *et al.* [1994] (square; $n = 8$). Numerical predictions of the canine LV models of Guccione *et al.* [39] (dashed) and Nash [40] (dash-dot) are also shown. Finally, numerical results using the present LV geometry and fibre structure with the Guccione constitutive model along path 1 are shown (dash-dot-dot).

DOI: 10.1002/cnm

The parameters of the Costa model have been fit by Schmid *et al.* [25] to the same experimental data used herein [15]. The resulting values are: $C = 0.26$ kPa, $b_{\mathrm{ff}} = 37.2$, $b_{\mathrm{fn}} = 12.0$, $b_{\mathrm{fs}} = 12.0$, $b_{\mathrm{nn}} = 9.11$, $b_{\mathrm{ns}} = 10.9$, and $b_{\mathrm{ss}} = 18.9$. The corresponding four parameters of the Guccione model, which were determined by Xi *et al.* [37] from the reparametrization of the Costa model by Schmid *et al.* [2008], are $C = 0.189$ kPa, $b_1 = 29.9$, $b_2 = 13.5$, $b_3 = 13.3$. Results obtained using these parameterizations of the Costa and Guccione constitutive models along with our LV geometry and fibre structure are shown in Figure 12. A comparison between results obtained with these Fung-type models and results obtained using the structure-based constitutive model is shown in Figure 13.

Figures 12 and 13 show that the two Fung-type models yield very similar results when used with the present LV geometry and fibre structure. However, there are large quantitative differences between the stress and strain distributions obtained by the Fung-type models and the structure-based constitutive model. In particular, the stress levels predicted by the Fung-type models are generally lower than those of the structure-based constitutive model, and the strains produced by both Fung-type models are much larger. These results suggest that overall stiffness of the LV model is higher using the structure-based model as compared to the Fung-type models.

6.6. Comparison to experimental data and computational models of canine hearts

Given the lack of published data on transmural strain distributions in the human LV, we compare the results of our model to published strain distributions from experimental studies of the canine heart [35, 36, 38]. To this end, in Figure 14, we display transmural strain data in the circumferential, radial, and longitudinal directions (see Figure 1 for definitions of the material coordinate system) using both the structure-based constitutive model and also the four-parameter Guccione model [20] using parameters of Xi *et al.* [37]. Results from corresponding canine models by Guccione *et al.* [39] and by Nash [40] are also shown. We remark that the study of Guccione *et al.* [39] also uses the Guccione constitutive model, although with different constitutive parameters. Although the geometry and fibre distributions of the canine heart are likely to be quite different from the present human model, there is an overall qualitative agreement between our model predictions and these canine results, especially for E_{cc}, E_{cl}, E_{ll} and E_{rr}. In addition, the predictions obtained using the present LV geometry and fibre structure but with the Guccione constitutive model seem to be in good agreement with the experimental observations for some strain components (e.g. E_{cr} and E_{lr}) but fail to reflect the radial changes for others (e.g. E_{cl} and E_{rr}). More detailed quantitative comparisons do not seem merited given the differences in geometry and constitutive parameters used in these simulations.

6.7. Discussion

Our results indicate that the fibre angle distribution can have a large impact on the stress distribution inside the left ventricular wall during diastole. In contrast, the sheet orientation has relatively minor effects on stress and strain distributions, at least during diastole. Close inspection of the results reveals that if the transmural range of fibre angles is relatively small (e.g. $R \approx 30°-40°$), the LV model has greater deformation in the longitudinal direction, whereas for a larger amount of transmural fibre rotation (e.g. $R \approx 70°-80°$), the LV becomes much stiffer in the longitudinal direction. This observation may be useful when developing procedures to estimate fibre distributions from *in vivo* observations of LV motion. We also find that if the fibre angle is further away from the normal case (e.g. away from $R = 60°$ and $T = 45°$), both the first principal stress and the stress in the fibre direction increase, thereby increasing the LV workload. This suggests that any pathological remodelling of the fibre distribution that reduces the amount of transmural fibre rotation may have a negative effect on heart function.

It is important to note that because our model is reconstructed from human cardiac MRI data, the geometry of the LV used in this work is not as regular as for some models used previously [28, 39]. This, in turn, will affect the stress and strain distributions. For example, in regions where the curvature change is greatest (e.g. path 4), the local fibre structure will change accordingly, and the stress distribution can differ markedly from that of neighbouring regions.

DOI: 10.1002/cnm

One limitation of our study is that we use porcine experimental data to determine the parameters of the constitutive model. The fibre structure is also rule-based, and may not reflect the fibre structure of the particular human LV used to construct the geometrical model. We also have not considered the roles of initial strains and residual stresses in our model, which both have the potential to alter the resultant stress and strain distributions. Finally, the current model treats the LV as a hyperelastic structure, without accounting for fluid–structure interactions, and the boundary conditions are therefore necessarily simplified. Further work is required to develop patient-specific fibre structure estimated from *in vivo* DTMR datasets, to evaluate the impact of initial strains and residual stresses, and to account for fluid–structure interaction. It is clear that closely matched experimental data are needed for more in-depth LV modelling.

7. CONCLUSIONS

In this work, we developed an anatomically realistic model of the human left ventricle that employs a structure-based constitutive model and a rule-based cardiac fibre distribution, and we used this model to simulate the diastolic mechanics of the heart. We treated the left ventricular myocardium as an inhomogeneous, thick-walled, nonlinearly elastic, incompressible material, following the modelling framework of Holzapfel and Ogden [5], which takes into account the fibre-reinforced microstructure of ventricular myocardium. By employing three independently developed sets of constitutive parameters, we found that the structure-based constitutive law employed here is relatively insensitive to small parameterization errors. The end-diastolic pressure–volume relationship of the model prediction agrees well with published *ex vivo* human heart measurements, but less well with measurements from canine hearts. We also found that changes in the sheet orientation had relatively little impact to the model results, whereas changes in the fibre angle distribution change the distributions of stress and strain dramatically. This highlights the importance of using realistic fibre structures, especially in pathological conditions that involve pathophysiological remodelling of fibre orientation. Finally, the transmural distributions of the stress and strain were compared with results obtained using other constitutive models, and with experimental measurements from canine hearts. We found large differences in the stress and strain predictions generated by the different constitutive models, even in cases in which the material parameters were fit to the same experimental data. In addition, although similar trends can be identified, our results are also different from published results from animal LV models. This highlights the significance of patient-specific modelling using *in vivo* imaging techniques to obtain an improved understanding of the physiology and pathophysiology of human hearts.

ACKNOWLEDGEMENTS

We gratefully acknowledge support from the Excellence Exchange Project funded by the Xi'an Jiaotong University, and support from the British Heart Foundation, the Medical Research Scotland, the Chief Scientist Office, the Scottish Funding Council and EPSRC grant EP/I02990. B.E.G. was supported in part by American Heart Association Scientist Development Grant 10SDG4320049 and by National Science Foundation Awards DMS 1016554 and OCI 1047734.

REFERENCES

1. Velagaleti RS, Pencina MJ, Murabito JM, Wang TJ, Parikh NI, D'Agostino RB, Levy D, Kannel WB, Vasan RS. Long-term trends in the incidence of heart failure after myocardial infarction. *Circulation* 2008; **118**(20):2057–2062.
2. Paulus WJ, Tschöpe C, Sanderson JE, Rusconi C, Flachskampf FA, Rademakers FE, Marino P, Smiseth OA, De Keulenaer G, Leite-Moreira AF. How to diagnose diastolic heart failure: a consensus statement on the diagnosis of heart failure with normal left ventricular ejection fraction by the Heart Failure and Echocardiography Associations of the European Society of Cardiology. *European Heart Journal* 2007; **28**(20):2539–2550.
3. Wang J, Nagueh SF. Current perspectives on cardiac function in patients with diastolic heart failure. *Circulation* 2009; **119**(8):1146–1157.
4. Wang VY, Lam HI, Ennis DB, Cowan BR, Young AA, Nash MP. Modelling passive diastolic mechanics with quantitative MRI of cardiac structure and function. *Medical Image Analysis* 2009; **13**(5):773–784.

DOI: 10.1002/cnm

5. Holzapfel GA, Ogden RW. Constitutive modelling of passive myocardium. A structurally-based framework for material characterization. *Philosophical Transactions of the Royal Society of London. Series A. Mathematical and Physical Sciences* 2009; **367**:3445–3475.
6. Hunter PJ, Nash MP, Sands GB. Computational electromechanics of the heart. *Computational Biology of the Heart* 1997:345–407.
7. LeGrice IJ, Smaill BH, Chai LZ, Edgar SG, Gavin JB, Hunter PJ. Laminar structure of the heart: ventricular myocyte arrangement and connective tissue architecture in the dog. *American Journal of Physiology- Heart and Circulatory Physiology* 1995; **269**(2):H571–H582.
8. Sands GB, Gerneke DA, Hooks DA, Green CR, Smaill BH, LeGrice IJ. Automated imaging of extended tissue volumes using confocal microscopy. *Microscopy Research and Technique* 2005; **67**(5):227–239.
9. Bishop M, Hales P, Plank G, Gavaghan D, Scheider J, Grau V. Comparison of rule-based and DTMRI-derived fibre architecture in a whole rat ventricular computational model. *Functional Imaging and Modeling of the Heart* 2009; **5528**:87–96.
10. Potse M, Dube B, Richer J, Vinet A, Gulrajani RM. A comparison of monodomain and bidomain reaction-diffusion models for action potential propagation in the human heart. *IEEE Transactions on Bio-medical Engineering* 2006; **53**(12):2425–2435.
11. Demer LL, Yin FC. Passive biaxial mechanical properties of isolated canine myocardium. *The Journal of Physiology* 1983; **339**(1):615.
12. Novak VP, Yin FCP, Humphrey JD. Regional mechanical properties of passive myocardium. *Journal of Biomechanics* 1994; **27**(4):403–412.
13. Smaill BH, Hunter PJ. Structure and function of the diastolic heart: material properties of passive myocardium. *Theory of Heart: Biomechanics, Biophysics and Nonlinear Dynamics of Cardiac Function* 1991:1–29.
14. Yin FCP, Strumpf RK, Chew PH, Zeger SL. Quantification of the mechanical properties of noncontracting canine myocardium under simultaneous biaxial loading. *Journal of Biomechanics* 1987; **20**(6):577–589.
15. Dokos S, Smaill BH, Young AA, LeGrice IJ. Shear properties of passive ventricular myocardium. *American Journal of Physiology-Heart and Circulatory Physiology* 2002; **283**(6):H2650–H2659.
16. Vossoughi J, Vaishnav RN, Patel DJ. Compressibility of the myocardial tissue. In *Advances in Bioengineering*, Mow VC (ed.). Bioengineering Division, American Society of Mechanical Engineers: New York, NY, 1980; 45–48.
17. Demiray H. Stresses in ventricular wall. *Journal of Applied Mechanics* 1976; **43**:194–197.
18. Costa KD, Hunter PJ, Rogers JM, Guccione JM, Waldman LK, McCulloch AD. A three-dimensional finite element method for large elastic deformations of ventricular myocardium: I—Cylindrical and spherical polar coordinates. *Journal of Biomechanical Engineering* 1996a; **118**:452–463.
19. Costa KD, Hunter PJ, Wayne JS, Waldman LK, Guccione JM, McCulloch AD. A three-dimensional finite element method for large elastic deformations of ventricular myocardium: II—prolate spheroidal coordinates. *Journal of Biomechanical Engineering* 1996b; **118**:464–472.
20. Guccione JM, McCulloch AD, Waldman LK. Passive material properties of intact ventricular myocardium determined from a cylindrical model. *Journal of Biomechanical Engineering* 1991; **113**:42–55.
21. Humphrey JD, Strumpf RK, Yin FCP. Determination of a constitutive relation for passive myocardium: I. A new functional form. *Journal of biomechanical engineering* 1990; **112**:333–339.
22. Humphrey JD, Strumpf RK, Yin FCP. Determination of a Constitutive Relation for Passive Myocardium: II.—Parameter Estimation. *Journal of biomechanical engineering* 1990; **112**:340–346.
23. Costa KD, Holmes JW, McCulloch AD. Modelling cardiac mechanical properties in three dimensions. *Philosophical Transactions of the Royal Society of London. Series A: Mathematical, Physical and Engineering Sciences* 2001; **359**(1783):1233–1250.
24. Schmid H, Nash MP, Young AA, Hunter PJ. Myocardial material parameter estimation—a comparative study for simple shear. *Journal of Biomechanical Engineering* 2006; **128**:742–750.
25. Schmid H, O'Callaghan P, Nash MP, Lin W, LeGrice IJ, Smaill BH, Young AA, Hunter PJ. Myocardial material parameter estimation. *Biomechanics and Modeling in Mechanobiology* 2008; **7**(3):161–173.
26. Horowitz A, Lanir Y, Yin FCP, Perl M, Sheinman I, Strumpf RK. Structural three-dimensional constitutive law for the passive myocardium. *Journal of Biomechanical Engineering* 1988; **110**:200–207.
27. Vetter FJ, McCulloch AD. Three-dimensional stress and strain in passive rabbit left ventricle: a model study. *Annals of Biomedical Engineering* 2000; **28**(7):781–792.
28. Nash MP, Hunter PJ. Computational mechanics of the heart. *Journal of Elasticity* 2000; **61**(1):113–141.
29. Stevens C, Remme E, LeGrice I, Hunter P. Ventricular mechanics in diastole: material parameter sensitivity. *Journal of Biomechanics* 2003; **36**(5):737–748.
30. Miehe C. Aspects of the formulation and finite element implementation of large strain isotropic elasticity. *International Journal for Numerical Methods in Engineering* 1994; **37**(12):1981–2004.
31. Göktepe S, Acharya SNS, Wong J, Kuhl E. Computational modeling of passive myocardium. *International Journal for Numerical Methods in Biomedical Engineering* 2011; **27**(1):1–12.
32. Buckberg GD, Weisfeldt ML, Ballester M, Beyar R, Burkhoff D, Coghlan HC, Doyle M, Epstein ND, Gharib M, Ideker RE. Left ventricular form and function. *Circulation* 2004; **110**(14):e333–e336.
33. Klotz S, Hay I, Dickstein ML, Yi GH, Wang J, Maurer MS, Kass DA, Burkhoff D. Single-beat estimation of end-diastolic pressure-volume relationship: a novel method with potential for noninvasive application. *American Journal of Physiology-Heart and Circulatory Physiology* 2006; **291**(1):H403–H412.

DOI: 10.1002/cnm

34. McCulloch AD, Hunter PJ, Smaill BH. Mechanical effects of coronary perfusion in the passive canine left ventricle. *American Journal of Physiology-Heart and Circulatory Physiology* 1992; **262**(2):H523–H530.
35. McCulloch AD, Smaill BH, Hunter PJ. Regional left ventricular epicardial deformation in the passive dog heart. *Circulation Research* 1989; **64**(4):721–733.
36. Omens JH, May KD, McCulloch AD. Transmural distribution of three-dimensional strain in the isolated arrested canine left ventricle. *American Journal of Physiology-Heart and Circulatory Physiology* 1991; **261**(3):H918–H928.
37. Xi J, Lamata P, Lee J, Moireau P, Chapelle D, Smith N. Myocardial transversely isotropic material parameter estimation from in-silico measurements based on a reduced-order unscented Kalman filter. *Journal of the Mechanical Behavior of Biomedical Materials* 2011; **4**(7):1090–1102.
38. May-Newman K, Omens JH, Pavelec RS, McCulloch AD. Three-dimensional transmural mechanical interaction between the coronary vasculature and passive myocardium in the dog. *Circulation Research* 1994; **74**(6):1166–1178.
39. Guccione JM, Costa KD, McCulloch AD. Finite element stress analysis of left ventricular mechanics in the beating dog heart. *Journal of Biomechanics* 1995; **28**(1):1167–1177.
40. Nash M. Mechanics and Material Properties of the Heart using an Anatomically Accurate Mathematical Model. *PhD thesis*, The University of Auckland, 1998.

DOI: 10.1002/cnm